International Journal of Mass Spectrometry 275 (2008) 34–44

Contents lists available at ScienceDirect

International Journal of Mass Spectrometry

journal homepage: www.elsevier.com/locate/ijms

# The elliptical Penning trap: Experimental investigations and simulations

Martin Breitenfeldt[a,*], Sudarshan Baruah[a], Klaus Blaum[b,c], Alexander Herlert[d], Martin Kretzschmar[b], Franklin Martinez[a], Gerrit Marx[a], Lutz Schweikhard[a], Noelle Walsh[a]

[a] Institut für Physik, Ernst-Moritz-Arndt-Universität, 17487 Greifswald, Germany
[b] Institut für Physik, Johannes Gutenberg-Universität, 55099 Mainz, Germany
[c] Gesellschaft für Schwerionenforschung GSI, Planckstrasse 1, 64291 Darmstadt, Germany
[d] Physics Department, CERN, 1211 Geneva 23, Switzerland

ARTICLE INFO

*Article history:*
Received 29 February 2008
Received in revised form 5 May 2008
Accepted 6 May 2008
Available online 15 May 2008

*Keywords:*
Ion storage
Penning trap
Ion motion
Frequency shift
FT-ICR MS

ABSTRACT

The application of an additional azimuthal quadrupolar electrostatic field to a Penning trap leads to a field configuration referred to as an elliptical Penning trap. The resulting changes of the radial ion motions have been investigated experimentally and by use of simulations. The eigenfrequencies, i.e., the magnetron frequency $\tilde{\omega}_-$ and the reduced cyclotron frequency $\tilde{\omega}_+$, are found to be shifted with respect to those of the standard Penning trap $\omega_-$, $\omega_+$, respectively. As the shift of the magnetron frequency $\tilde{\omega}_-$ is larger than that of the reduced cyclotron frequency $\tilde{\omega}_+$ their sum $\tilde{\omega}_+ + \tilde{\omega}_-$ is also a function of the ellipticity and no longer equal to the cyclotron frequency in the absence of an electric trapping field $\omega_c = qB/m$. The frequency shifts were investigated for argon and fullerene ions. The experimental studies were performed by time-of-flight (ToF) analysis of the ion cyclotron resonance and by Fourier-transform ion-cyclotron-resonance mass spectrometry (FT-ICR MS). The experimental and simulated values are in agreement with theoretical predictions [M. Kretzschmar, this issue] when the influence of higher multipole terms is taken into account.



## 1. Introduction

The storage of charged particles in a small volume [1,2] allows various investigations as, e.g., in the fields of analytical (bio-)chemistry [3,4], ion-molecule reactions [5,6], delayed photodissociation [7] as well as mass spectrometry of stable and short-lived nuclides [8,9]. In general, a thorough understanding of the applied trapping device is required for its successful application. To this end, various ion trapping and detection methods have been invented and further developed over the years. In the case of Penning traps these include FT-ICR MS (Fourier-transform ion-cyclotron-resonance mass spectrometry) [10,11], the detection of the cyclotron resonance frequency by measuring the reduction of the time of flight (ToF) to an external ion detector [12,13], dipolar and quadrupolar excitations [13–15], and buffer gas cooling (axialization) [16,17] to name a few.

In the present work a specific variation of the electrostatic potential is investigated: the elliptical Penning trap [18], where an additional azimuthal quadrupolar field is added to the electric trapping field of the standard Penning trap, in analogy to earlier considerations for the Paul trap [19,20]. The resulting configuration is thus similar to the "trapped ion analyzer cell" [21], which preceded the transition from earlier ICR "drift cell" techniques to FT-ICR MS. For the case of a small perturbation an additional azimuthal quadrupolar component has been treated earlier with respect to the invariance of the sum of squared frequencies of the eigenmotions [22,23]. In contrast, the present work investigates azimuthal quadrupolar components up to the limit of ion-motion stability. The effect of the additional field on the radial ion motion is probed with argon and fullerene ions. The results are compared to theoretical predictions and to simulations of the ion trajectories. A full account of the theory of the elliptical Penning trap is given by M. Kretzschmar in a separate article of this volume [24]. Note that these investigations are performed with respect to the ion motion of single trapped particles. A study of the influence of an azimuthal quadrupolar field on the diocotron frequency of an electron plasma can be found in ref. [25].

## 2. Ion motion in a Penning trap

### 2.1. Conventional Penning trap

In a conventional Penning trap [23] particles with mass $m$ and charge $q$ are stored in a superposition of a homogeneous magnetic

* Corresponding author.
*E-mail address:* martin.breitenfeldt@cern.ch (M. Breitenfeldt).

1387-3806/$ – see front matter © 2008 Elsevier B.V. All rights reserved.
doi:10.1016/j.ijms.2008.05.008

field $\vec{B} = (0, 0, B)$ and an electrostatic axial quadrupolar field for radial and axial confinement, respectively. The electrostatic potential is of the form:

$$\Phi(x, y, z) = \frac{U_0}{2d^2}\left(z^2 - \frac{r^2}{2}\right) + \Phi_0, \tag{1}$$

with $r = \sqrt{x^2 + y^2}$ and a potential difference $U_0$ applied between the hyperbolical endcap and ring electrodes. With a radius $r_0$ of the ring electrode and a distance $z_0$ of the endcaps from the center, the trap dimension $d$ is given by

$$d^2 = \frac{1}{2}\left(z_0^2 + \frac{r_0^2}{2}\right). \tag{2}$$

As in the following, we are only concerned with the ion motion inside the trap, the overall offset of the trap potential $\Phi_0$ can be neglected. A stored ion is moving with three independent motional modes: an oscillation in the axial direction (trapping motion) with the (angular) frequency

$$\omega_z = \sqrt{\frac{qU_0}{md^2}} \tag{3}$$

and two radial modes (cyclotron motion and drift motion) with the reduced cyclotron frequency $\omega_+$ and the magnetron frequency $\omega_-$, respectively,

$$\omega_\pm = \tfrac{1}{2}(\omega_c \pm \omega_1), \tag{4}$$

where

$$\omega_c = \frac{q}{m}B \tag{5}$$

is the cyclotron frequency in the absence of the electric field and $\omega_1$ is defined as

$$\omega_1 = \sqrt{\omega_c^2 - 2\omega_z^2}. \tag{6}$$

In other contexts [26,27] this frequency has been denoted as the parametric frequency $\omega_p$.

The stability condition of the radial motion $\omega_c^2 > 2\omega_z^2$ leads to an upper limit of the mass-to-charge ratio:

$$\frac{m}{q} < \left(\frac{m}{q}\right)_{crit} = \frac{d^2B^2}{2U_0}. \tag{7}$$

With this ratio, the Penning trap parameter

$$\Pi = \frac{m/q}{(m/q)_{crit}} = 2\frac{\omega_z^2}{\omega_c^2}; \tag{8}$$

can be defined. It is a dimensionless parameter, which characterizes the trapping condition of the ion motion [28]. For the standard Penning trap, the stability range extends from $\Pi = 0$ to $\Pi = 1$. As shown below, this range is increased for elliptical traps or alternatively, a modified Penning trap parameter $\tilde{\Pi}$ can be introduced.

### 2.2. Elliptical Penning trap

In the case of an elliptical Penning trap an additional quadrupolar potential

$$\Phi_{ellipt} = a_{2,0} \cdot c_2 \frac{U_{ellipt}}{r_0^2}(x^2 - y^2) \tag{9}$$

is added to the standard electrostatic potential (Eq. (1)). $U_{ellipt}$ is the additional voltage applied to the different segments of the ring electrode (see Section 3). The coefficients $a_{2,0}$ and $c_2$ are introduced to describe the influence of the particular electrode configurations: The coefficent $c_2$ is derived from a Fourier transform of the voltages applied to the ring segments as a function of the azimuthal angle. For the present configuration (see below) this coefficient is $c_2 \simeq 1.45$. As the ring has a finite extension and the azimuthal quadrupolar field is not applied to the endcaps (as e.g., the dipolar field of an "infinity cell" [29]) the effect of the $U_{ellipt}$ on the ring electrodes is reduced. $a_{2,0}$ quantifies this shielding influence of the endcaps. For asymptotically symmetric traps ($r_0^2 = 2z_0^2$ and thus $d^2 = z_0^2 = r_0^2/2$) [30] a numerical calculation gives $a_{2,0} \simeq 0.78$ (see below). The axial part of the potential energy

$$E_z(z) = \tfrac{1}{2}m\omega_z^2 z^2 \tag{10}$$

remains unchanged by the $\Phi_{ellipt}$ contribution. The radial part can be rewritten as [24]

$$E_r(x, y) = -\tfrac{1}{4}m\omega_z^2((1-\epsilon)x^2 + (1+\epsilon)y^2), \tag{11}$$

where the parameter

$$\epsilon = a_{2,0} \cdot c_2 \frac{2U_{ellipt}}{U_0} \tag{12}$$

shall be denoted as "ellipticity". Four cases can be distinguished (Fig. 1):

- $\epsilon = 0$: Standard Penning trap: The equipotential lines in the $xy$-plane are circles.
- $0 < |\epsilon| < 1$: The equipotential lines are more or less stretched ellipses.
- $|\epsilon| = 1$: The equipotential lines distort to straight lines (no ion confinement).
- $|\epsilon| > 1$: A saddle with hyperbolic equipotential lines is generated (no ion confinement).

The radial eigenfrequencies of the elliptical Penning trap are predicted as [24]:

$$\tilde{\omega}_\pm = \sqrt{\frac{1}{2}(\omega_c^2 - \omega_z^2) \pm \frac{1}{2}\sqrt{\omega_c^2\omega_1^2 + \epsilon^2\omega_z^4}}, \tag{13}$$

which, when expanded for $\tilde{\omega}_-$ in $\omega_z^2/\omega_c^2$, yields the known relation [23]

$$\tilde{\omega}_- = \frac{\omega_z^2}{2\omega_c^2}\sqrt{1 - \epsilon^2}, \tag{14}$$

whereas the axial frequency remains unchanged, $\tilde{\omega}_z = \omega_z$.

Here and in the following, symbols without tilde refer to the ideal Penning trap (no additional quadrupolar potential), symbols with tilde refer to the elliptical Penning trap. The trapping frequency $\omega_z$ is related to the radial frequencies by

$$\omega_z^2 = 2\omega_+\omega_- = \frac{2\tilde{\omega}_+\tilde{\omega}_-}{\sqrt{1 - \epsilon^2}}. \tag{15}$$

Furthermore, by squaring Eq. (13) the invariance theorem [22,23] is recovered:

$$\tilde{\omega}_+^2 + \tilde{\omega}_-^2 + \tilde{\omega}_z^2 = \omega_+^2 + \omega_-^2 + \omega_z^2 = \omega_c^2. \tag{16}$$

The values $\epsilon = \pm 1$ mark the transition to an imaginary frequency $\tilde{\omega}_-$, i.e., the end of stable magnetron orbits in the elliptical Penning trap. They correspond to a maximum of the applied elliptical potential $U_{ellipt}$ at the ring segments of

$$U_{ellipt}^{(max)} = \frac{U_0}{2a_{2,0} \cdot c_2}. \tag{17}$$

For $\epsilon \neq 0$ the upper limit of the charge-to-mass ratio is denoted by $\widetilde{(m/q)}_{crit}$. It is obtained from the condition $\omega_c^2\omega_1^2 + \epsilon^2\omega_z^4 = 0$ (see

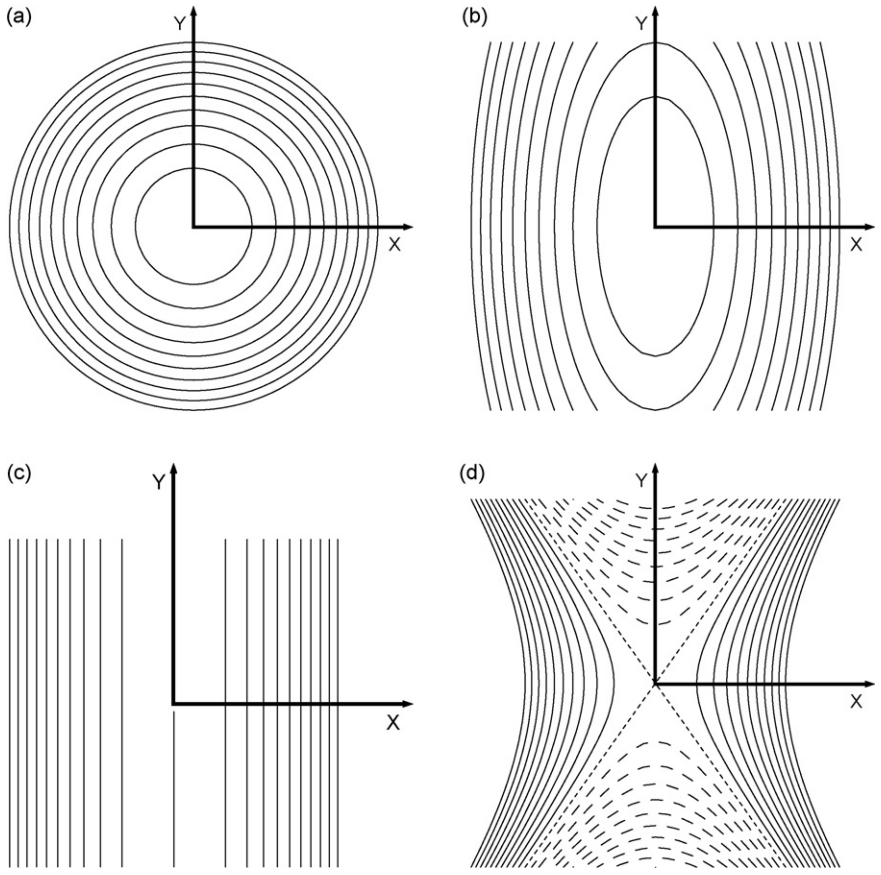


**Fig. 1.** Equidistant equipotential lines in the $z = 0$ plane for different values of $\epsilon$. (a) $\epsilon = 0$, (b) $\epsilon = -0.8$, (c) $\epsilon = -1$ and (d) $\epsilon = -2$ (full lines and dashed lines for negative and positive values, respectively).

Eq. (13)) as

$$\widetilde{\left(\frac{m}{q}\right)}_{\text{crit}} = \frac{d^2B^2}{2U_0} \cdot \frac{2}{\left(1+\sqrt{1-\epsilon^2}\right)} = \left(\frac{m}{q}\right)_{\text{crit}} \cdot \frac{2}{\left(1+\sqrt{1-\epsilon^2}\right)}. \tag{18}$$

This results in an increase of the critical mass-to-charge ratio $(\widetilde{m/q})_{\text{crit}}$ as compared to that of the standard Penning trap (Eq. (7)). The Penning trap parameter $\widetilde{\Pi}$ therefore depends on the ellipticity and becomes

$$\widetilde{\Pi} = \frac{m/q}{(\widetilde{m/q})_{\text{crit}}} = \frac{m/q}{(m/q)_{\text{crit}}} \frac{1+\sqrt{1-\epsilon^2}}{2} = \frac{\omega_z^2}{\omega_c^2}(1+\sqrt{1-\epsilon^2})$$

$$= \Pi \cdot \frac{(1+\sqrt{1-\epsilon^2})}{2}. \tag{19}$$

Thus, the maximum value of $\Pi$ varies from 1 to 2 as $|\epsilon|$ varies from 0 to 1, while $\widetilde{\Pi}$ is again a dimensionless parameter between 0 and 1.

By use of $\Pi$, as defined in Eq. (8), the eigenfrequencies can be expressed as:

$$\frac{\tilde{\omega}_z}{\omega_c} = \frac{\omega_z}{\omega_c} = \sqrt{\frac{\Pi}{2}}, \tag{20}$$

$$\frac{\tilde{\omega}_\pm}{\omega_c} = \frac{1}{2}\sqrt{2-\Pi \pm 2\sqrt{1-\Pi+\frac{1}{4}\epsilon^2\Pi^2}}. \tag{21}$$

Fig. 2 shows the dependence of the eigenfrequencies on the Penning trap parameter $\Pi$ for three different ellipticities: $\epsilon = 0$, 0.8 and 1. Beyond the point where the magnetron frequency $\tilde{\omega}_-$ and the reduced cyclotron frequency $\tilde{\omega}_+$ considered, e.g., as functions of the mass of the trapped particle become equal, i.e., beyond $\tilde{\omega}_- = \tilde{\omega}_+$, the trapping condition Eq. (7) can not be satisfied.

The influence of the ellipticity represented by $\epsilon$ on the ion orbits can be described by introducing the semi-major axes are $\tilde{R}_{-\text{maj}}$ and

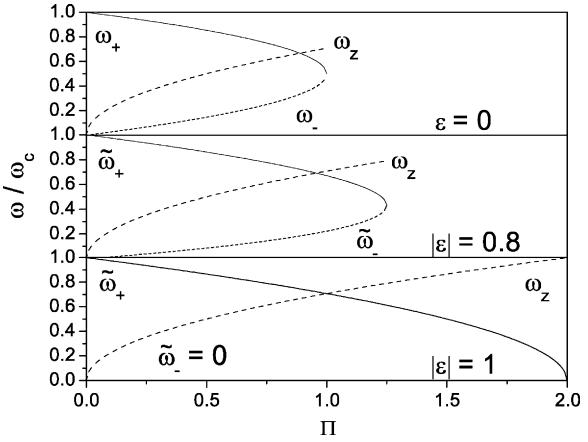


**Fig. 2.** The frequency ratios $\omega_z/\omega_c$, $\tilde{\omega}_+/\omega_c$, and $\tilde{\omega}_-/\omega_c$ as a function of the Penning trap parameter $\Pi$ for ellipticities $\epsilon = 0$, (top), $|\epsilon| = 0.8$, (center), and $|\epsilon| = 1$, (bottom). In the lowest plot the magnetron frequency is equal to zero.

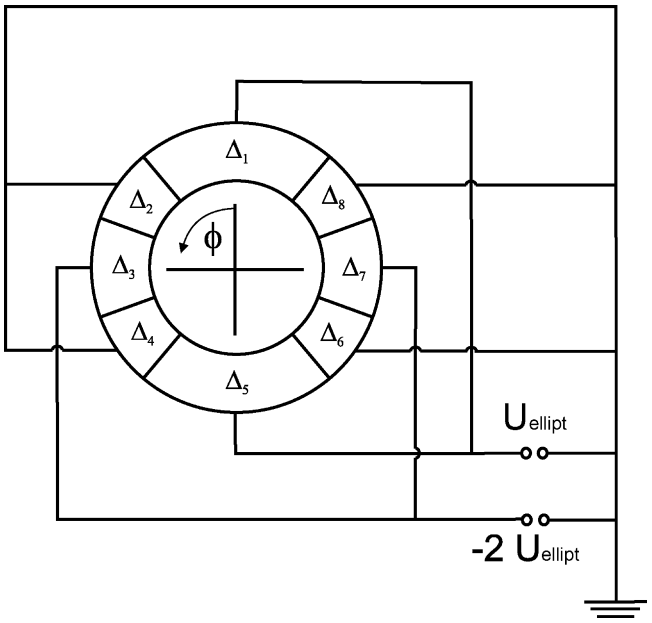


**Fig. 3.** DC connections to the ring segments of ClusterTrap in case of the elliptical Penning trap.

$\tilde{R}_{+\mathrm{maj}}$ of the ion orbits [24]:

$$\tilde{R}_{\pm\mathrm{maj}} = \tilde{R}_{\pm} \cdot \sqrt{\frac{\omega_c^2 + |\epsilon|\omega_z^2 \pm \sqrt{\omega_c^2\omega_1^2 + \epsilon^2\omega_z^4}}{2(\tilde{\omega}_{\pm}/\omega_1)\cdot\sqrt{\omega_c^2\omega_1^2 + \epsilon^2\omega_z^4}}}. \tag{22}$$

In analogy, the semi-minor axises is given by:

$$\tilde{R}_{\pm\min} = \tilde{R}_{\pm} \cdot \sqrt{\frac{\omega_c^2 - |\epsilon|\omega_z^2 \pm \sqrt{\omega_c^2\omega_1^2 + \epsilon^2\omega_z^4}}{2(\tilde{\omega}_{\pm}/\omega_1)\cdot\sqrt{\omega_c^2\omega_1^2 + \epsilon^2\omega_z^4}}}. \tag{23}$$

For the cyclotron motion the difference between $\tilde{R}_+$, $\tilde{R}_{+\mathrm{maj}}$ and $\tilde{R}_{+\min}$ is less than 0.1% for the maximum ellipticity $\epsilon = 1$, so in the scope of the current investigation we will assume $\tilde{R}_+ = \tilde{R}_{+\mathrm{maj}} = \tilde{R}_{+\min}$. The resulting ion trajectories are illustrated in Section 5, below.

## 3. Experimental setup and procedure

The experiments were performed at ClusterTrap [31,32] (now at Greifswald, Germany), a setup for the investigation of small metal clusters [33–35] and fullerenes [36], and the study of ion manipulation in Penning traps [26,37–44]. It comprises an ion source, a transfer section, a Penning trap with hyperbolically shaped electrodes ($r_0 = 20\,\mathrm{mm}$, $r_0^2 = 2z_0^2$), a superconducting magnet ($B = 4.97\,\mathrm{T}$), and a time-of-flight section with a conversion-electrode micro-channel-plate detector for mass analysis. For most of the present measurements a potential $U_0 = 10\,\mathrm{V}$ was applied between the ring electrode and the two endcap electrodes for ion storage.

### 3.1. Elliptical Penning trap

The ring electrode is segmented with the dividing slits at the angular coordinates $\phi_1, \phi_2, \ldots, \phi_8 = \phi_0$ [26,37] (see Fig. 3) in order to allow the application of various radiofrequency (rf) excitations, e.g., dipolar, quadrupolar, or octupolar rf fields [44], for the manipulation of the ion motion [27]. The sizes of the segments are denoted by $\Delta_i = \phi_i - \phi_{i-1}$ for $i = 1, \ldots, 8$ and the voltages $U_i$ were applied to the segments. At ClusterTrap there are two pairs of opposing

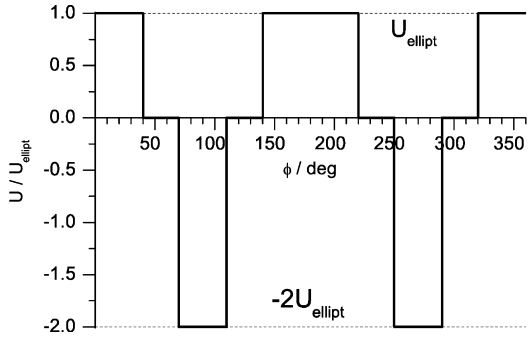


**Fig. 4.** The DC voltages (normalized to the voltage at segment 1) applied to the segmented ring electrode as a function of the azimuthal angle $\phi$.

segments, $\Delta_1 = \Delta_5 = 80^\circ$ and $\Delta_3 = \Delta_7 = 40^\circ$, separated by four $\Delta_2 = \Delta_4 = \Delta_6 = \Delta_8 = 30^\circ$ segments.

The voltages were chosen such that their average potential contribution on the ring electrode was zero:

$$\sum_{n=1}^{8} U_n \cdot \Delta_n = 2 \cdot U_1 \cdot 80^\circ + 4 \cdot U_2 \cdot 30^\circ + 2 \cdot U_3 \cdot 40^\circ = 0, \tag{24}$$

with $U_5 = U_1$ and $U_7 = U_3$. Frequency shifts due to a change of the axial potential well and the trapping potential depth are therefore avoided. With the four 30° segments on ground potential ($U_2 = U_4 = U_6 = U_8 = 0$) this results in a configuration with $U_3 = -2U_1$ as plotted in Fig. 4. In the following $U_1$ is identified with $U_{\mathrm{ellipt}}$.

For a comparison of the effect of $U_{\mathrm{ellipt}}$ with the theoretical prediction, the coefficient $c_2$ has to be calculated for the present geometry by a Fourier analysis of the radial potential. The origin of the angular coordinates is set in the middle of segment 1 such that $\phi_1 = \Delta_1/2$ and $\phi_0 = -\Delta_1/2$ so that $\Delta_1 = \phi_1 - \phi_0$. Furthermore, $\phi_7 = 2\pi - \phi_2$, $\phi_6 = 2\pi - \phi_3$, and $\phi_5 = 2\pi - \phi_4$ (Fig. 4). The potential function $U(\phi)$ thus acquires the symmetry properties $U(\phi) = U(-\phi)$ and $U(\phi) = U(\phi + \pi)$. For the Fourier expansion of $U(\phi)$ the first symmetry property implies that the Fourier series is a pure cosine series, the second property permits only terms depending on even multiples of $\phi$. Thus for the current geometry the Fourier expansion of the potential of the ring electrode assumes the form

$$U(\phi) = \sum_{n=0}^{\infty} u_{2n}\cos(2n\phi) = U_{\mathrm{ellipt}} \sum_{n=0}^{\infty} c_{2n}\cos(2n\phi), \tag{25}$$

with the dimensionless Fourier coefficients $c_{2n}$.

The condition (24) requires $c_0 = 0$. The Fourier components are given by

$$\begin{aligned} u_{2n} &= \frac{1}{\pi}\int_{-\pi}^{+\pi} \mathrm{d}\phi \cdot U(\phi)\cos(2n\phi) \\ &= \frac{1}{n\pi}\sum_{i=1}^{4} U_i \cdot (\sin(2n\phi_i) - \sin(2n\phi_{i-1})) \\ &= \frac{2}{n\pi}[(U_1 - U_2)\cdot\sin(n\Delta_1) + (U_3 - U_2)\cdot(-1)^n\sin(n\Delta_3)] \\ &= \frac{2}{n\pi}[U_{\mathrm{ellipt}}\cdot\sin(n\cdot 80^\circ) - 2U_{\mathrm{ellipt}}\cdot(-1)^n\sin(n\cdot 40^\circ)]. \end{aligned} \tag{26}$$

The resulting first 16 Fourier coefficients are listed in Table 1.

The frequency shift caused by the additional azimuthal quadrupolar field was probed via the excitation of the radial ion motion and the measurement of the resonance frequencies. The

**Table 1**
Fourier coefficient for the ClusterTrap setup (to six significant digits)

| | |
|---|---|
| $c_2 = +1.44537$ | $c_{18} = 0$ |
| $c_4 = -0.51808$ | $c_{20} = -0.01915$ |
| $c_6 = +0.18378$ | $c_{22} = +0.13379$ |
| $c_8 = -0.21117$ | $c_{24} = -0.13783$ |
| $c_{10} = -0.00525$ | $c_{26} = +0.00202$ |
| $c_{12} = +0.27564$ | $c_{28} = +0.06033$ |
| $c_{14} = -0.21023$ | $c_{30} = -0.03676$ |
| $c_{16} = +0.02393$ | $c_{32} = +0.06476$ |

dipolar excitation signal was achieved by a function generator (Stanford Research System, model DS345) and a home-built phase splitter. It was applied to two opposing 30° segments with opposite polarity. For the quadrupolar excitation a second rf signal was produced by another function generator and the amplitude was increased by use of an rf amplifier (ENI, model 2100L). The signal was applied on the other two 30° segments with the same polarity [18,45]. Two different detection schemes were used as described in the following.

### 3.2. Time-of-flight effect measurements on fullerene ions

Fullerene ions were produced in an external ion source [36] by the evaporation of neutral fullerenes in an oven. After electron impact ionization they were transferred to the Penning trap by use of electrostatic ion-optical elements. For the capture and accumulation the kinetic energy of the ions was chosen such that the ions just passed the endcap potential and afterwards lost energy due to collisions with argon buffer gas inside the trap. The buffer gas background pressure was kept constant in the order of $10^{-5}$ Pa. The fullerene ion beam was gated by deflectors with typical accumulation periods of 700 ms in order to prevent an interaction with the stored ions during the following experimental steps. In addition, mass-selective centering and cooling was applied [16].

The frequencies $\tilde{\nu}_+$ and $\tilde{\nu}_-$ were determined by monitoring the time of flight (ToF) of the ions from the trap to the detector as a function of the frequency of the applied rf excitation [12,14]. In resonance, the orbital magnetic moment

$$\vec{\mu} = I \cdot \vec{A} = q\frac{\omega}{2\pi} \cdot \pi R_+^2 \tag{27}$$

is increased due to the larger amplitude of the cyclotron motion, the radius $R_+$. $\vec{A}$ is the area enclosed by the ion trajectory. Thus, in resonance, the magnetic energy of the ions

$$E_r = -\vec{\mu} \cdot \vec{B} \tag{28}$$

is increased as well. (Note that $\vec{\mu}$ and $\vec{B}$ have opposite directions.) When the ions are axially ejected from the trap, they experience an accelerating force towards the detector as they drift through the magnetic field gradient [46]:

$$\vec{F} = \vec{\nabla}(\vec{\mu} \cdot \vec{B}). \tag{29}$$

Accordingly, particles with a larger magnetic moment $\mu$ arrive earlier at the detector than particles with a smaller $\mu$ [12]. The difference in the ToF for resonantly and non-resonantly excited ions (ToF effect) depends on the radius and the frequency of the ion motion. For the excitation of the cyclotron motion the ToF effect can be measured directly. In the case of the excitation of the magnetron motion, however, the magnetic moment is too small to yield a measurable ToF effect. Therefore, the magnetron motion is converted to cyclotron motion [13] by a broadband quadrupolar excitation before the ions are ejected from the trap. Similarly, the resonance frequency for this quadrupolar excitation, namely the sum of the reduced cyclotron and the magnetron frequency, can be determined by first giving the ions a defined magnetron radius (via a dipolar excitation at the magnetron frequency) and then applying the quadrupolar rf signal for conversion of the motional modes. This is the approach taken in precision mass measurements on short-lived radionuclides at a resolving power exceeding a million [8,9]. In the present investigation, the damping by collisions with residual buffer gas has limited the resolution of the ToF-effect measurements.

### 3.3. FT-ICR measurements on argon ions

The frequency shifts have also been probed with $Ar^+$. The ions were produced in the trap volume by electron-impact ionization of argon atoms. This production method has somewhat less well-defined initial conditions for the ion position and kinetic energy as compared to the case of fullerenes, since argon buffer gas cooling cannot be applied. However, it allowed the generation of a larger number of ions and therefore the analysis of the ion motion using FT-ICR mass spectrometry. This method has been further applied in a recent study of FT-ICR monitoring of various excitation schemes [44].

In the present work, the image current induced by the revolving ions was picked up via the two opposing 80° ring segments and fed into a home-built differential amplifier. The signal was recorded by a spectrum analyzer (Stanford Research Systems, model SR760). This device has a relatively small memory size (1 kB), which limits the resolving power of the signal in the frequency domain. With a sampling frequency of 100 kHz, the frequency range extends only to a Nyquist limit [47] of 50 kHz. Therefore, this method was limited to the determination of the magnetron frequency.

## 4. Results

The expected dependence of eigenfrequencies $\tilde{\nu}_\pm = \tilde{\omega}_\pm/(2\pi)$ on $U_{\text{ellipt}}$ for the present experimental settings is shown in Fig. 5. In the case of $Ar^+$ and $C_{60}{}^+$ the maximum frequency shift is expected to be $\Delta\nu_{+\max} = \tilde{\nu}_+ - \nu_+ = 168$ mHz and 3 Hz, respectively. Therefore, $\tilde{\nu}_+$ can be considered to be constant within the uncertainty of the present study. In contrast, the shift of the magnetron frequency $\Delta\nu_{-\max} = \tilde{\nu}_- - \nu_-$ is about two orders of magnitude larger. Consequently, the $\nu_-$ shift can be monitored by measuring the sum frequency $\tilde{\nu}_+ + \tilde{\nu}_- = \tilde{\nu}_{\text{conv}}$ at which the conversion from the magnetron into the cyclotron motion takes place [13].

### 4.1. Time-of-flight effect measurements

For the determination of the reduced cyclotron frequency $\tilde{\nu}_+$ in the elliptical Penning trap the cyclotron motion was excited with a radial dipolar rf field for $T_{\text{ex}} = 30$ ms and the resulting time of flight of the $C_{60}$ ions was measured as a function of the excitation frequency. In Fig. 6, two $\tilde{\nu}_+$ resonances for elliptical potentials $U_{\text{ellipt}} = 0$ V and $U_{\text{ellipt}} = 2.5$ V are shown. As expected no shift of the eigenfrequency is observed within the uncertainties of the order of 2 Hz as determined from the resonance curves fitted with a Gaussian.

The change of the conversion frequency $\tilde{\nu}_{\text{conv}} = \tilde{\nu}_+ + \tilde{\nu}_-$ was determined as a function of the elliptical potential by scanning the frequency $\nu_{\text{rf}}$ of the quadrupolar rf excitation after dipolar excitation of the magnetron mode at the appropriate frequency $\tilde{\nu}_-$. The magnetron motion was excited in dipolar geometry for a period of $T_{\text{ex}} = 10$ ms at an amplitude of $U_{\text{ex}} = 10\,V_{\text{pp}}$, where for each excitation the frequency was adjusted to match the expected magnetron frequency. Due to the gated rf excitation, the excitation frequency was Fourier broadened with a width of about $\Delta\nu_{\text{rf}} = 100$ Hz and the actual magnetron frequency was always maintained well within

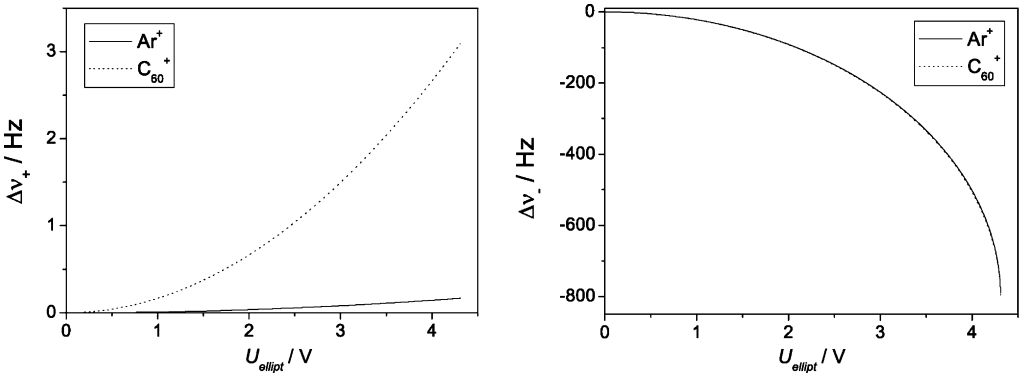


**Fig. 5.** Frequency shifts predicted by Eqs. (12) and (13) $\Delta\nu_+ = \tilde{\nu}_+ - \nu_+$ (left) and $\Delta\nu_- = \tilde{\nu}_- - \nu_-$ (right) for $Ar^+$ and $C_{60}^+$ as a function of the ellipticity voltage. With the parameters $U_0 = 10$ V, $B_0 = 4.97$ T, $a_{2,0} = 0.78$, $c_2 = 1.45$ the unshifted frequencies are $\nu_+ = 1907.1$ kHz and $\nu_- = 800.9$ Hz for $Ar^+$, and $\nu_+ = 105.2$ kHz and $\nu_- = 806.8$ Hz for $C_{60}^+$, respectively. Note that the curves for the expected frequency shift $\Delta\nu_-$ are almost identical.

that range. In Fig. 7 two resonances for the determination of $\tilde{\nu}_{conv}$ at the elliptical potentials $U_{ellipt} = 0$ V and $U_{ellipt} = 2.5$ V are shown for $C_{60}^+$. As the magnetron frequency is given by $\tilde{\nu}_- = \tilde{\nu}_{conv} - \tilde{\nu}_+$ and $\tilde{\nu}_+$ is almost constant (see above) the observed shift is practically identical with the shift of the magnetron frequency.

In addition, the shift of the magnetron frequency was measured in the more direct way, i.e., by frequency scans of the dipolar excitation at the magnetron frequency. Since the magnetic moment of the low-frequency magnetron motion is too small to produce a measurable ToF effect, a subsequent conversion from magnetron to cyclotron motion was added, as in the previous experiment, i.e., by the application of a quadrupolar excitation at $\tilde{\nu}_{conv}$. The frequency $\tilde{\nu}_{conv}$ was adjusted for each elliptical voltage $U_{ellipt}$, in analogy with $\tilde{\nu}_-$ in the previous experiment. In addition, a fast conversion in 10 ms was used to broaden the excitation bandwidth.

The measured frequency shifts of $\tilde{\nu}_-$ and $\tilde{\nu}_{conv}$ are plotted in Fig. 8 for elliptical potentials from 0 to 3.5 V. The two ordinate scales

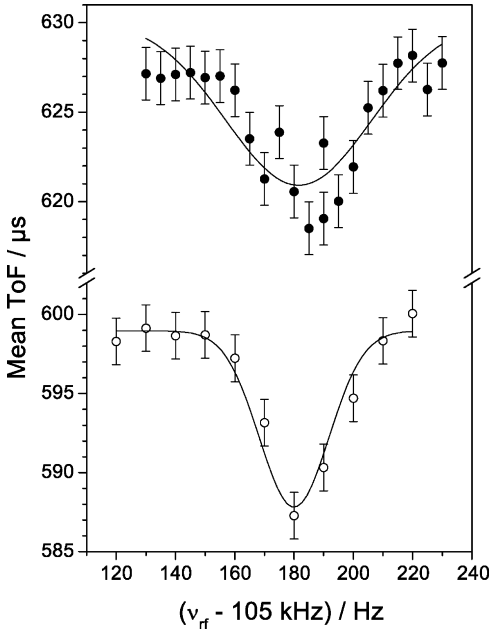


**Fig. 6.** ToF resonances of $C_{60}^+$ for the determination of $\tilde{\nu}_+$, i.e., mean ToF as a function of the frequency for dipolar excitation, with $U_{ellipt} = 0$ (bottom, open circles) and $U_{ellipt} = 2.5$ V (top, filled circles), superposed on the trapping potential $U_0 = 10$ V. The error bars indicate the standard deviation of the mean ToF. The difference for the base line of the mean ToF is due to the different values of the electrostatic potentials applied to the deflectors and lenses in the TOF section.

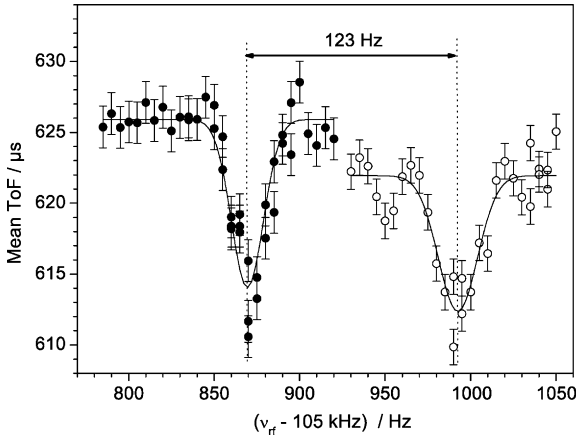


**Fig. 7.** Mean ToF of $C_{60}^+$ as a function of the quadrupolar excitation frequency (after dipolar excitation of the magnetron motion) for the determination of $\tilde{\nu}_{conv} = \tilde{\nu}_+ + \tilde{\nu}_-$ at $U_{ellipt} = 0$ V (open circles) and $U_{ellipt} = 2.5$ V (filled circles) at trap parameters as in Fig. 6.

are shifted towards each other by the value of the reduced cyclotron frequency $\nu_+ = 105.18$ kHz of the standard Penning trap ($U_{ellipt} = 0$). For values $U_{ellipt} \geq 4.0$ V, i.e., $U_{ellipt}/U_0 \geq 0.4$, it was not possible to store a sufficient number of ions such that measurements could be performed. Apparently, for these conditions the potentials and

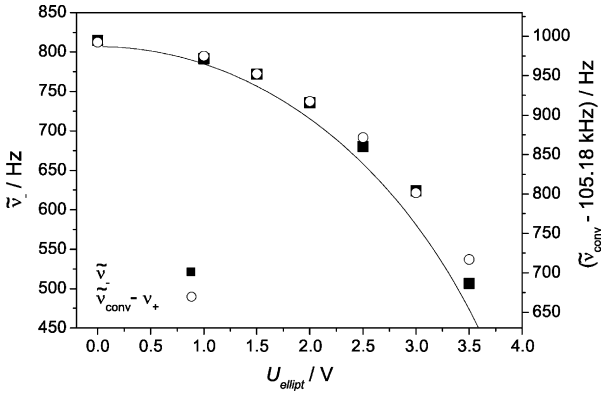


**Fig. 8.** Measured magnetron frequency $\tilde{\nu}_-$ (filled squares) and conversion frequency $\tilde{\nu}_{conv} = \tilde{\nu}_- + \tilde{\nu}_+$ (open circles) of $C_{60}^+$ as a function of $U_{ellipt}$. Note that the scales are shifted relative to each other by a constant value of $\nu_+ = 105.18$ kHz, i.e., the reduced cyclotron frequency of the standard Penning trap. The statistical uncertainty is smaller than the symbol size. The solid line shows the expected behavior according to Eq. (13).

thus the ion trajectories are to distorted for extended storage times (compare also Fig. 10, below).

### 4.2. FT-ICR measurements

In an independent series of measurements the shift of the magnetron frequency of $Ar^+$ was probed by use of FT-ICR MS, i.e., $\tilde{\nu}_-$ was deduced from a transient of the ions' image current. As above, a gated rf excitation ($T_{rf} = 10$ ms) was applied, which leads to broad-band excitation with $\Delta\nu_{rf} \cong 100$ Hz. In addition, the excitation frequency was adjusted to match the expected magnetron frequency.

The observed signal frequency is plotted as a function of the elliptical potential in Fig. 9. The measurements were performed for three different trapping potentials: $U_0 = 10$, 20 and 30 V. In order to compare the results, the magnetron frequency and the elliptical voltage are normalized to $U_0 = 10$ V, i.e., $\tilde{\nu}_-(U_0) \cdot 10\,\text{V}/\,U_0$ is plotted versus $U_{\text{ellipt}} \cdot 10\,\text{V}/\,U_0$. As deduced from the graph, the magnetron frequency decreases for higher elliptical potential and the reduction scales with the trapping potential.

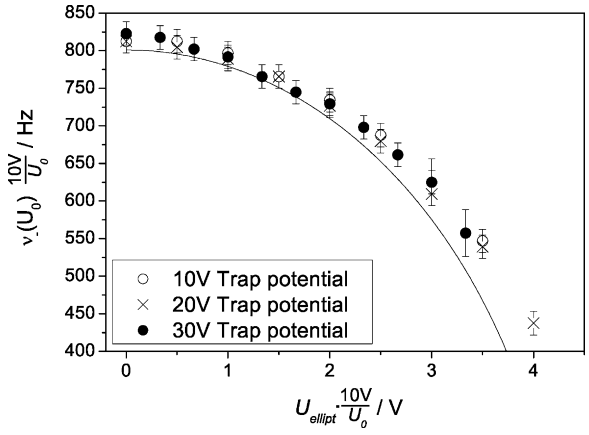


**Fig. 9.** Magnetron frequency of $Ar^+$ at $U_0 = 10$, 20 and 30 V as a function of $U_{\text{ellipt}}$ as measured by the FT-ICR technique. The values of $\tilde{\nu}_-$ and $U_{\text{ellipt}}$ have been rescaled to a 10-V trap potential. Solid line as in Fig. 8.

## 5. Simulation

The elliptical Penning trap has been further investigated by simulations with SIMION (version 3D 7.0) [48]. The geometry of the hyperbolically shaped electrodes as well as the magnitude of the magnetic field have been matched to the experimental conditions: The ring electrode is divided into two 80°, two 40°, and four 30° segments (see Fig. 3 and Fig. 10), the radius of the ring electrode is $r_0 = 2$ cm, the distance between the endcaps is $2z_0 = \sqrt{2}r_0 = 2.83$ cm, and the trapping potential is $U_0 = 10$ V. The grid step size applied for the numerical calculations was 0.5 mm.

As in the corresponding experimental studies, the elliptical voltage $U_{\text{ellipt}}$ was applied in the following way: the 80° segments were set to $U_{\text{ellipt}}$ and the 40° segments to $-2 \cdot U_{\text{ellipt}}$, while the 30° segments were on ground potential. In this case the Fourier coefficient is $c_2 \simeq 1.45$ (Table 1). The equipotential lines for four different values of $U_{\text{ellipt}}$ are plotted for the $z = 0$ plane in Fig. 10.

In a standard Penning trap the trajectory of the ion motion is a superposition of two circular motions as shown in Fig. 11 (part a

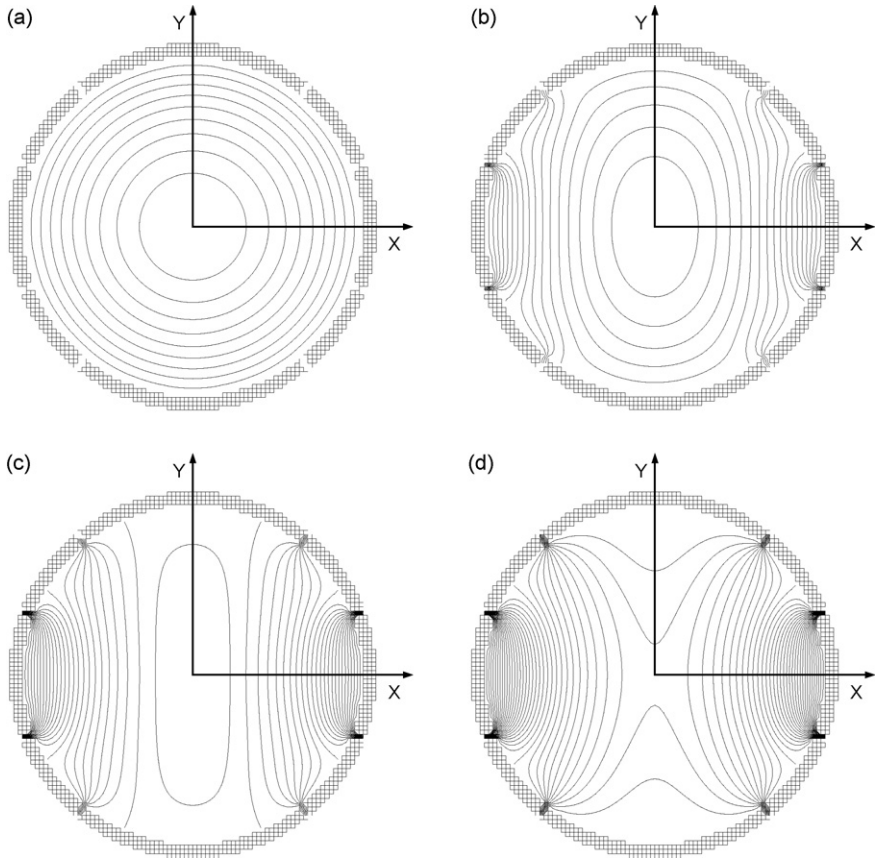


**Fig. 10.** Equipotential lines in the plane $z = 0$ for different ellipticity voltages $U_{\text{ellipt}}$ (calculations performed with SIMION 7.0). (a) $U_{\text{ellipt}} = 0$ V, (b) $U_{\text{ellipt}} = 2$ V, (c) $U_{\text{ellipt}} = 4$ V, and (d) $U_{\text{ellipt}} = 6$ V with $U_0 = 10$ V. The equipotential lines have an equidistant separation of 0.5 V.

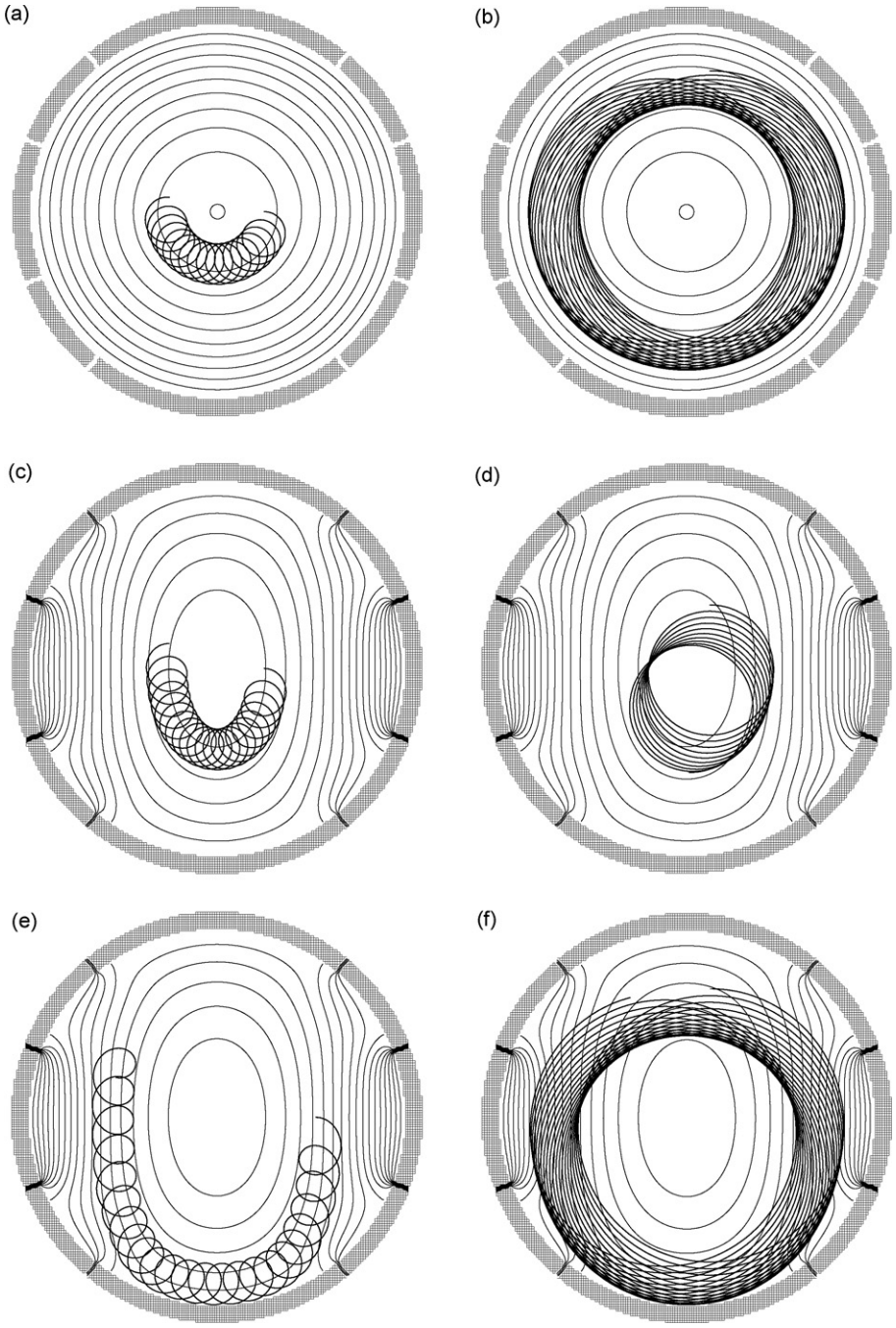


**Fig. 11.** Equipotential lines and trajectories for an ion of mass-to-charge ratio $m/q = 10\,000$ in the plane $z = 0$ for the standard Penning trap with $U_{\text{ellipt}} = 0$ V (a and b), and for the elliptical Penning trap with $U_{\text{ellipt}} = 2$ V (c–f). For comparison of the magnetron and the cyclotron motion $\tilde{R}_{-\text{maj}} > R_+$ is plotted in (a), (c), (e) and $\tilde{R}_{-\text{maj}} < R_+$ in (b), (d), (f).

and b). In the present case an ion with mass-to-charge ratio $m/q = 10000$ has been used to clarify the change of the ion trajectory as a function of the ellipticity, since the radial eigenfrequencies $\nu_- = 0.9$ kHz and $\nu_+ = 6.7$ kHz are of a similar order of magnitude. The radii have been chosen to be $R_- \approx 7$ mm $> R_+ \approx 2$ mm (Fig. 11(a)) and $R_- \approx 2$ mm $< R_+ \approx 15$ mm (Fig. 11(b)). In both cases the ion follows the equipotential lines with its magnetron motion while, in addition, performing cyclotron cycles.

When $U_{\text{ellipt}}$ is applied, the ions still follow the equipotential lines with their magnetron motion and move on an elliptical orbit as shown in Fig. 11(c) for $\tilde{R}_{-\text{maj}} \approx 7$ mm $> R_+ \approx 2$ mm. The distortion of the cyclotron orbit is predicted to be orders of magnitude smaller than that of the magnetron orbit (Section 2.2). Fig. 11(d) confirms this prediction; the cyclotron orbit can still be well described by a constant radius $R_+ \approx 7$ mm.

Fig. 11(e) shows a case with $\tilde{R}_{-\text{maj}} \approx 15$ mm close to the trap radius $r_0 = 20$ mm. The ion still follows the equipotential lines with the magnetron motion. The magnetron orbit deviates from an elliptical shape due to higher multipole terms of the particular electrode configuration. In contrast, large cyclotron orbits with $R_+ \approx 16$ mm are still well approximated by circles (Fig. 11(f)).

The eigenfrequency of the magnetron motion has been probed for ions with $m/q = 720$ ($C_{60}^+$) and $m/q = 40$ ($Ar^+$), which were positioned 1 mm radially off the trap center along the semi-major

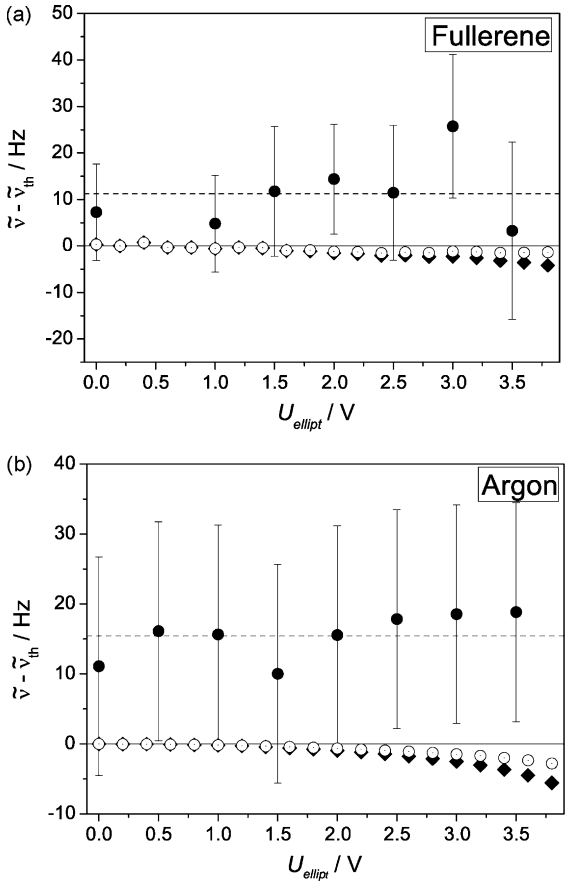


**Fig. 12.** The deviation of the experimental data (full circles) and of the simulated values (open circles) from the values predicted by theory for the magnetron frequency, Eq. (30), as a function of $U_{\text{ellipt}}$ for (a) fullerene and (b) argon ions. The dashed line indicates an offset of 11.2 and 15.5 Hz, respectively. The filled diamonds show the difference between simulation and theory for the azimuthal quadrupolar component, only, (Eq. (13)). The simulation values are adjusted by a constant offset of 3 Hz each to match the theory value at $U_{\text{ellipt}} = 0$. This offset is probably due to the finite grid spacing of the simulations.

axis. The initial kinetic energy was set to $E_{\text{kin}} = 0$ eV, i.e., the initial velocity was $\vec{v}_+ + \vec{v}_- = 0$ or $\vec{v}_+ = -\vec{v}_-$. The contribution of the cyclotron mode to the ion trajectory can be neglected. The magnetron frequency is deduced from the period of a full revolution. The difference between the resulting magnetron frequency and the theoretically predicted values is calculated using Eq. (30) and is plotted as a function of $U_{\text{ellipt}}$ in Fig. 12 (full diamonds).

## 6. Discussion

The systematic shift between the measured frequencies and the simulated values of 10–16 Hz for both, $Ar^+$ and fullerene ions, (see Fig. 12) is probably due to deviations of a few percent of the experimental trapping parameters $U_0$ and $d^2$ as compared to the assumed values, for example $\Delta U_0 \simeq 0.2$ V at $U_0 = 10$ V or $\Delta d^2 \simeq 6\,\text{mm}^2$ at $d^2 = 200\,\text{mm}^2$. Apart from this shift there is a good agreement between the simulated values and the experimental data, both for the ToF-effect measurements in case of the fullerene ions and for the FT-ICR measurements on $Ar^+$ ions. For potentials $U_{\text{ellipt}} < 2$ V the simulated values coincide with the theoretical predictions for the ideal elliptical Penning trap, Eq. (13).

For larger values of $U_{\text{ellipt}}$ a difference between simulated and theoretical values as predicted by Eq. (13) can be observed. This indicates an influence of higher order multipole terms, which (in analogy to the quadrupole term) cause an additional frequency shift. The difference can be estimated by theory as described in ref. [24]. using only the lowest order term for each $n$ we find

$$\Delta\tilde{\omega}_\pm = \pm\frac{2qU_{\text{ellipt}}}{m\omega_1 r_0^2}\sum_{n=2}^{\infty} a_{2n,0}\cdot c_{2n}\cdot\frac{(2n-1)!!}{(n-1)!}\cdot\frac{r_0^2}{\tilde{R}_\pm^2}\cdot\left[\frac{\text{sign}(\epsilon)\left(\tilde{R}_{\pm\text{maj}}^2-\tilde{R}_{\pm\,\text{min}}^2\right)}{2r_0^2}\right]^n, \quad (30)$$

where $a_{2n,0}$ gives the reduction of the strength of the $2n$-pole term by the presence of the endcaps. For higher order approximations see [24].

The eigenfrequency $\tilde{\nu}_-$ as a function of the applied voltage $U_{\text{ellipt}}$ was also determined by a SIMION [48] simulation. It included higher order terms, their coefficients were obtained as described in ref. [13]. To represent the $2n^{\text{th}}$ multipole the ring electrode was split into $2n$segments, where each segment had approximately a angle size of $[(360/2n) - 1]$ degrees. Note that the difference of 1° is required by the software. The potential applied to the endcaps was $V_{\text{ec}} = 0$ V. The multipolar azimuthal potential was achieved by applying ±1 V to the neighboring ring segments. The potential was read out in a grid of $20 \times 20 \times 20$ points. These 8000 points were distributed equally in a cube with an edge length of 60% of the ring radius $r_0$, where one corner was placed in the center of the trap and three edges were aligned along the axis of of the Cartesian coordinate system.

The first three terms of the multipole expansion in spherical coordinates

$$\Phi_{2n} = V_{2n}\cos(2n\varphi)\sum_{m=0}^{2}\left(a'_{2n,2m}\left(\frac{r}{r_0}\right)^{2n+2m}P_{2n+2m}^{2n}(\cos\theta)\right), \quad (31)$$

where $P_l^k(\cos\theta)$ are the associated Legendre polynomials and the coefficients $a'$ describe the strength of the multipoles, were fitted to the potential of the simulation.

Note that a transformation of this equation into Cartesian coordinates shows the symmetry in $z$ of the terms with $2n$. The terms with $2n+1$ are anti-symmetric in $z$, thus they do not contribute to the expansion of the potential:

$$\Phi_n = \Phi c_{2n}\left(\frac{a_{2n,0}}{r_0^{2n}}\cdot\Re((x+\text{i}y)^{2n}) + \frac{a_{2n,2}}{r_0^{2n+2}}\cdot\Re((x+\text{i}y)^{2n})(r^2-\alpha_n z^2) + \frac{a_{2n,4}}{r_0^{2n+4}}\cdot\Re((x+\text{i}y)^{2n})(r^4-\beta_n z^2 r^2+\gamma_n z^4)+\ldots\right). \quad (32)$$

The coefficients $a$ are adjusted with factors deduced from associated Legendre polynomials and the geometrical factor from the Fourier analysis is calculated separately to $c_{2n} = 4/\pi$. Note that this factor is different from the values given in Table 1 due to the different geometry. The coefficients $\alpha_n = 2(n+1)$, $\beta_n = 8(n+1)$, and $\gamma_n = 8/3(n+1)(2n+1)$ are obtained by an expansion of the associated Legendre functions. The resulting functions were adjusted by least-square minimization to the potentials as calculated with SIMION. The resulting coefficients $a$ are shown in Table 2. The 1st order coefficient $a_{2,0}$ differs by less than 5% to that published in ref. [13], i.e., $a_{2,0} = 0.78$ instead of 0.80, while the higher order coefficient shows a somewhat larger deviation. Note that this method is limited to lower multipole terms. The functions are fitted in a range of $r/r_0$ between 0 and 0.6. Especially for the higher multipole terms, where $r/r_0$ goes with the $n^{\text{th}}$ power, a significant number of grid points do not contribute to the fitting procedure. Thus the present values should be taken as a rough estimate.

**Table 2**
Coefficients for the influence of the endcaps on the trap potential

| $a_{2n,0}$ | $a_{2n,2}$ | $a_{2n,4}$ |
|---|---|---|
| $a_{1,0} = 0.70$ | $a_{1,2} = 0.42$ | $a_{1,4} = 0.07$ |
| $a_{2,0} = 0.78$ | $a_{2,2} = 0.24$ | $a_{2,4} = 0.04$ |
| $a_{4,0} = 0.77$ | $a_{4,2} = 0.14$ | $a_{4,4} = 0.04$ |
| $a_{6,0} = 0.78$ | $a_{6,2} = 0.15$ | $a_{6,4} = 0.05$ |
| $a_{8,0} = 0.65$ | $a_{8,2} = 0.13$ | $a_{8,4} = 0.04$ |
| $a_{10,0} = 0.78$ | $a_{10,2} = 0.16$ | $a_{10,4} = 0.05$ |

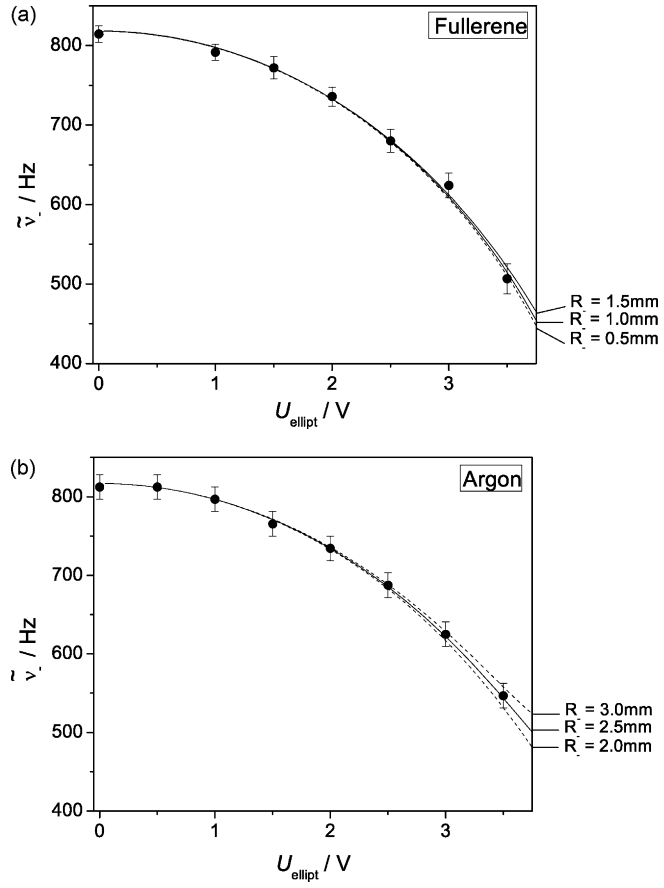


**Fig. 13.** Theoretical predictions of $\tilde{\nu}_-$ for different $\tilde{R}_-$ (solid and dashed lines) and experimental data (full circles) as a function of $U_{ellipt}$. (A constant offset of 11.2 and 15.5 Hz (see Fig. 12), respectively, was added to theoretical curves when determining the radius.)

The difference between the simulated values and those calculated from theory, which includes the higher-order terms up to a dodecapolar potential, are displayed in Fig. 12 as open circles as a function of $U_{ellipt}$. For comparison the difference of the magnetron frequency $\tilde{\nu}_-$ from the FT-ICR measurement with $Ar^+$ and the ToF-effect measurement with $C_{60}^+$ to the theoretical predictions by Eq. (30) are plotted as well (full circles). Note that unlike the frequency shift due to the quadrupole component $\Delta\tilde{\omega}_-$ depends on the "radii" $\tilde{R}_{-\mathrm{maj}}$ and $\tilde{R}_{-\mathrm{min}}$. This dependency allows the determination of the experimental $R_-$ value to about 2.5 mm and 1 mm, respectively, as calculated using Eq. (30) and shown in Fig. 13.

## 7. Conclusion

The influence of an additional azimuthal quadrupolar electrostatic field on the eigenfrequencies of ions in a Penning trap has been investigated. The eigenfrequencies of argon ions, $Ar^+$, and fullerene ions, $C_{60}^+$, were probed with the FT-ICR technique and the ToF-effect method, respectively. For the magnetron motion a shift to smaller frequency values was observed, which is in agreement with theoretical predictions as well as ion trajectory simulations. The discrepancies between an ideal elliptical Penning trap and the present measurements can be explained by contributions of higher multipole terms.

The investigations are part of a continued study of the fundamentals of ion storage and excitation of the ion motions with the belief that such endeavors eventually improve the understanding as well as the applicability of ion trapping devices. The present investigations allow an estimate of possible shifts of the eigenfrequencies of ions in Penning traps due to additional azimuthal quadrupolar terms. Especially in the case of high-precision mass spectrometry of short-lived nuclides [8,9], where relative mass uncertainties of up to $\delta m/m = 10^{-8}$ are required, it is important to know the influence of a distortion of the potential to the motional frequencies. As an example, in the case of $Ar^+$ and for the present experimental parameters, a distortion of the potential of $U_{ellipt} = 1$ mV, would result in a frequency shift of $\delta\nu_c = \nu_c - (\tilde{\nu}_+ + \tilde{\nu}_-) = 0.5$ mHz corresponding to a relative shift of only $\delta\nu_c/\nu_c = 2.5 \times 10^{-10}$, i.e., well below the present limits for mass measurements of radionuclides, but already significant in the case of the even lower uncertainty achieved for stable particles [49].

A very different application could be found in the field of photodissociation of, e.g., cluster ions [50], where one of the apices (i.e., the endpoints of the semi-major axis) of the magnetron trajectory could be used as a defined location of the particle-laser interaction region. Similar arguments can be made for other interactions such as electron bombardment or the location for axial injection of precursor ions or ejection of products.

The present work has studied the ion behavior in static elliptical field components. In addition, by switching the voltage $U_{ellipt}$ the ion motion could be manipulated: Depending on the ion position (i.e., the phase of the ion motion) at the moment of switching, the ions can be transferred to a smaller or larger magnetron radius.

Yet other possibilities may emerge when the interaction of several ions is taken into account, which is outside of the scope of the present study. One speculation, e.g., would be that in combination with the technique of the "ion balance" [49,51], where the eigenmotions of two particles couple, the elliptical Penning trap could be used to "park" the ions, since the elliptical equipotential trajectories would provide a situation at the apices where the repelling force between the two ions is minimal.

## Acknowledgements

This work was supported by the Sonderforschungsbereich SFB652 of the Deutsche Forschungsgemeinschaft, the German Ministry for Education and Research (BMBF) under contract 06GF186I, and the GSI research and development program. K. Blaum acknowledges support by the Helmholtz association of research centres under contract VH-NG-037. Furthermore, the authors thank the Max-Planck-Institute for Plasma Physics, IPP, Greifswald, for its kind hospitality.

## Appendix A

In the case of FT-ICR measurements one works with a large number of ions, which induce image charges in the electrodes resulting in shifts of the eigenfrequencies. For circular orbits in a standard Penning trap (i.e., for pure cyclotron motion or pure magnetron

motion) the frequency shift can be estimated [52] by

$$\omega_{\pm,\mathrm{image}} = \frac{\omega_c}{2} \pm \sqrt{\left(\frac{\omega_c}{2}\right)^2 - \frac{\omega_z^2}{2} - \omega_{\mathrm{image}}^2} \approx \omega_\pm \mp \frac{\omega_{\mathrm{image}}^2}{\omega_1} \tag{33}$$

with

$$\omega_{\mathrm{image}}^2 = \frac{Nq^2}{m} \cdot \frac{r_0}{(r_0^2 - R_\pm^2)^2}, \tag{34}$$

where $N$ is the number of ions, $R_\pm$ the radius of the ion orbit, and $r_0 - R_\pm$ the distance of the ion from the ring electrode. Ions that are far out from the center of the trap experience a larger shift than those with smaller orbital radii.

In the elliptical Penning trap we have (for pure cyclotron or for pure magnetron motion) elliptical instead of circular ion orbits. Thus the distance of the ion from the ring electrode varies along the orbit. For the pure motional modes the shifts of the eigenfrequencies can then be estimated [24] by means of a generalization of Eq. (33)

$$\Delta\tilde{\omega}_\pm = \mp \frac{Nq^2}{2m\omega_1 r_0^3} \cdot \frac{\tilde{R}_{\pm\mathrm{maj}}^2 + \tilde{R}_{\pm\,\mathrm{min}}^2 - 2\tilde{R}_{\pm\mathrm{maj}}^2 \tilde{R}_{\pm\,\mathrm{min}}^2 / r_0^2}{\tilde{R}_\pm^2 [(1 - \tilde{R}_{\pm\mathrm{maj}}^2/r_0^2)(1 - \tilde{R}_{\pm\,\mathrm{min}}^2/r_0^2)]^{3/2}}. \tag{35}$$

Assuming $N = 10^5$, an orbital parameter $\tilde{R}_- = 2.5$ mm corresponding to the adjusted value of our FT-ICR measurements, and an ellipticity $\epsilon < 0.7$ this formula yields a magnetron frequency shift due to image charges of less than 1 mHz. Therefore, for the ion orbits investigated in our measurements this effect is negligible.

## References


[1] P.K. Ghosh, Ion Traps (International Series of Monographs on Physics, vol. 90), Clarendon Press, 1995.
[2] F.G. Major, V.N. Gheorghe, G. Werth, Charged Particle Traps: Physics and Techniques of Charged Particle Field Confinement, Springer, Berlin, 2004.
[3] M. Bronstrup, Mod. Mass Spectrom. 225 (2003) 283.
[4] R.M.A. Heeren, A.J. Kleinnijenhuis, L.A. McDonnell, T.H. Mize, Anal. Bioanal. Chem. 378 (2004) 1048.
[5] H. Schwarz, Angew. Chem. Int. Ed. 42 (2003) 4442.
[6] D.K. Boehme, H. Schwarz, Angew. Chem. Int. Ed. 44 (2005) 2336.
[7] R.C. Dunbar, Int. J. Mass Spectrom. 200 (2000) 571.
[8] K. Blaum, Phys. Rep. 425 (2006) 1.
[9] L. Schweikhard, G. Bollen (Eds.), Int. J. Mass Spectrom. 251 (2006) (Special issue).
[10] M.B. Comisarow, A.G. Marshall, Chem. Phys. Lett. 25 (1974) 282.
[11] A.G. Marshall, C.L. Hendrickson, G.S. Jackson, Mass Spectrom. Rev. 17 (1998) 1.
[12] G. Gräff, H. Kalinowsky, J. Traut, Z. Phys. A 297 (1980) 35.
[13] G. Bollen, R.B. Moore, G. Savard, H. Stolzenberg, J. Appl. Phys. 68 (1990) 4355.
[14] M. König, G. Bollen, H.-J. Kluge, T. Otto, J. Szerypo, Int. J. Mass Spectrom. Ion Processes 142 (1995) 95.
[15] K. Blaum, G. Bollen, F. Herfurth, A. Kellerbauer, H.-J. Kluge, M. Kuckein, S. Heinz, P. Schmidt, L. Schweikhard, J. Phys. B 36 (2003) 921.
[16] G. Savard, St. Becker, G. Bollen, H.-J. Kluge, R.B. Moore, Th. Otto, L. Schweikhard, H. Stolzenberg, U. Wiess, Phys. Lett. A 158 (1991) 247.
[17] L. Schweikhard, S. Guan, A.G. Marshall, Int. J. Mass Spectrom. Ion Processes 120 (1992) 71.
[18] L. Schweikhard, M. Breitenfeldt, A. Herlert, F. Martinez, G. Marx, N. Walsh, in: M. Drewsen, U.I. Uggerhoj, H. Knudson (Eds.), Non-Neutral Plasma Physics VI, AIP Conference Proceedings, vol. 862, New York, 2006, p. 264.
[19] W. Paul, H. Steinwedel, Z. Naturf. 8a (1953) 448.
[20] W. Paul, H.P. Reinhard, U.V. Zahn, Z. Phys. 152 (1958) 143.
[21] R.T. McIver, Rev. Sci. Instrum. 41 (1970) 555.
[22] L.S. Brown, G. Gabrielse, Phys. Rev. A 25 (1982) 2423.
[23] L.S. Brown, G. Gabrielse, Rev. Mod. Phys. 58 (1986) 233.
[24] M. Kretzschmar, Int. J. Mass Spectrom. 275 (2008) 21.
[25] J. Fajans, E. Gilson, E.Y. Backhaus, Phys. Plasma 7 (2000) 3929.
[26] L. Schweikhard, M. Lindinger, H.-J. Kluge, Rev. Sci. Instrum. 61 (1990) 1055.
[27] L. Schweikhard, A.G. Marschall, J. Am. Soc. Mass. Spectrom. 4 (1993) 433.
[28] L. Schweikhard, J. Ziegler, H. Bopp, K. Lützenkirchen, Int. J. Mass Spectrom. Ion Processes 141 (1995) 77.
[29] P. Caravatti, M. Allemann, Org. Mass Spectrom. 26 (1991) 514.
[30] R.D. Knight, Int. J. Mass Spectrom. Ion Phys. 51 (1983) 127.
[31] St. Becker, K. Dasgupta, G. Dietrich, H.-J. Kluge, S. Kuznetsov, M. Lindinger, K. Lützenkirchen, L. Schweikhard, J. Ziegler, Rev. Sci. Instrum. 66 (1995) 4902.
[32] L. Schweikhard, S. Krückeberg, K. Lützenkirchen, C. Walther, Eur. Phys. J. D 9 (1999) 15.
[33] L. Schweikhard, St. Becker, K. Dasgupta, G. Dietrich, H.-J. Kluge, D. Kreisle, S. Krückeberg, S. Kuznetsov, M. Lindinger, K. Lützenkirchen, B. Obst, C. Walther, H. Weidele, J. Ziegler, Phys. Scripta T59 (1995) 236.
[34] L. Schweikhard, A. Herlert, M. Vogel, in: E.E.B. Campbell, M. Larsson (Eds.), The Physics and Chemistry of Clusters, World Scientific, Singapore, 2001, p. 267.
[35] L. Schweikhard, A. Herlert, G. Marx, K. Hansen, in: J.-P. Connerade, A.V. Solovyov (Eds.), Latest Advances in Atomic Clusters Collision: Atomic Cluster Collisions: Fission, Fusion, Electron, Ion and Photon Impact, Imperial College Press, World Scientific, London, 2004, p. 85.
[36] A. Lassesson, N. Walsh, F. Martinez, A. Herlert, G. Marx, L. Schweikhard, Eur. Phys. J. D (2005) 73.
[37] L. Schweikhard, M. Lindinger, H.-J. Kluge, Int. J. Mass Spectrom. Ion Processes 98 (1990) 25.
[38] H.-U. Hasse, St. Becker, G. Dietrich, N. Klisch, H.-J. Kluge, M. Lindinger, K. Lützenkirchen, L. Schweikhard, J. Ziegler, Int. J. Mass Spectrom. Ion Processes 132 (1994) 181.
[39] L. Schweikhard, J. Ziegler, P. Beiersdorfer, B. Beck, S. Becker, S.R. Elliott, Rev. Sci. Instrum. 66 (1995) 448.
[40] L. Schweikhard, P. Beiersdorfer, W. Bell, G. Dietrich, S. Krückeberg, K. Lützenkirchen, B. Obst, J. Ziegler, Hyperfine Interact. 99 (1996) 97.
[41] A. Herlert, S. Krückeberg, L. Schweikhard, M. Vogel, C. Walther, Phys. Scripta T80 (1999) 200.
[42] A. Herlert, L. Schweikhard, M. Vogel, in: F. Anderegg, L. Schweikhard, C.F. Driscoll (Eds.), Non-neutral plasma physics IV. AIP Conference Proceedings, vol. 606, 2002, p. 652.
[43] A. Herlert, L. Schweikhard, Int. J. Mass Spectrom. 234 (2004) 161.
[44] M. Breitenfeldt, F. Ziegler, A. Herlert, G. Marx, L. Schweikhard, Int. J. Mass Spectrom. 263 (2007) 94.
[45] C.L. Hendrickson, J.J. Drader, D.A. Laude, J. Am. Soc. Mass Spectrom. 6 (1995) 97.
[46] J.D. Jackson, Classical Electrodynamics, John Wiley & Sons Inc., London, 1963.
[47] A.G. Marshall, F.R. Verdun, Fourier Transforms in NMR Optical and Mass Spectrometry: A User's Handbook, Elsevier Science Ltd., New York, 1990.
[48] D.A. Dahl, SIMION 3D 7.0, Laplace Equation Solver Software, Idaho National Engeneering Laboratory.
[49] S. Rainville, J.K. Thompson, D.E. Pritchard, Science 303 (2004) 334.
[50] C. Walther, G. Dietrich, M. Lindinger, K. Lützenkirchen, L. Schweikhard, J. Ziegler, Chem. Phys. Lett. 256 (1996) 77, and 262 (1996) 668.
[51] E.A. Cornell, K.R. Boyce, D.L.K. Fygenson, D.E. Pritchard, Phys. Rev. A 45 (1992) 3049.
[52] R.S. Van Dyck, F.L. Moore, D.L. Farnham, P.B. Schwinberg, Phys. Rev. A 40 (1989) 6308.